Electronic Supporting Information

Solvent control: Dinuclear versus tetranuclear complexes of a bis-tetradentate pyrimidine-based ligand

Worku A. Gobeze,[a] Victoria A. Milway,[a] Boujemaa Moubaraki,[b] Keith S. Murray,[b] and Sally Brooker[a]*

[a] Department of Chemistry and the MacDiarmid Institute for Advanced Materials and Nanotechnology, University of Otago, P.O. Box 56, Dunedin 9054, New Zealand

[b] School of Chemistry, Monash University, PO Box 23, Clayton, Victoria 3800, Australia

Instrumentation and Measurements

Elemental analyses were carried out by the Campbell Microanalytical Laboratory at the University of Otago. ^{1}H, ^{13}C and ^{19}F NMR spectra were recorded on a Varian INOVA 500 spectrometer at 25°C. Electrospray spectra (ES-MS) were collected at the University of Otago on a Shimadzu QP8000 alpha with APCI/ESI probes. Infrared spectra were recorded on a Perkin Elmer Spectrum BX FT-IR system in the range 4000-400 cm^{-1} samples pressed potassium bromide discs or using directly the powder sample with FT-ATR spectrometer with an Alpha-P module. UV/Vis spectra were recorded on a Varian CARY 500 Scan UV/VIS/NIR spectrophotometer, using quartz curvettes with a 1 cm pathlength, in the range 200-1200 nm. Molar conductivities were measured with a Suntex SC-170 conductivity meter with 1mM solutions of the compounds. Cyclic voltammetric studies were carried out in 0.1 M of tetraethylammonium hexafluorophosphate and 0.1 mM of compound in acetonitrile, if not stated otherwise. A classical three-electrode cell was used (a platinum working electrode, a platinum counter electrode and an $Ag/AgNO_3$ reference electrode), connected to a computerized electrochemical device EG & G Princeton Applied Research, Potentiostat/Galvanostat Model 273A. As a reference check, ferrocene was added at the conclusion of each experiment.

Magnetic measurements

For all cases the measurements were carried out on powder samples. The measurements for the complexes **2**, **3**, **4** and **9** were carried out on a Quantum Design PPMS 5 SQUID magnetometer with the sample (~20 mg) contained in a gelatine capsule in Monash, Australia. The measurement for **8** was made on a Quantum Design MPMS-XL 7T SQUID magnetometer, with the sample contained in a gelatin capsule, while **10** was measured on the Quantum Design 9T PPMS using the Vibrating Sample Magnetometer, with the sample contained in polypropylene capsule, both at IRL, Wellington, New Zealand. In all cases the data were corrected for the signal of the sample holder and the diamagnetic contribution of the sample, using Pascal's tables. The measurements for **8** and **10** were carried out in a field of 1 Tesla (10,000 Oe) while complexes **2**, **3**, **4** and **9** were measured in a field 0.5 Tesla. Unless otherwise stated, the temperature range for the measurements was 300-2 K.

X-ray crystallography

General: All non-hydrogen atoms were modelled anisotropically except where noted. Hydrogen atoms were inserted at calculated positions and rode on the non-H atoms to which they are attached (including isotropic thermal parameters which were equal to 1.2 times to the attached non-hydrogen atom), except where noted, when hydrogen atoms were instead either located from the difference map or inserted at positions suggested by SHELXL-97 and then their coordinates fixed. Notes on the details of each structure are detailed in below.

Table S1: is now Table 4 in the main body of the paper.

$[Mn^{II}_2L^{Et}(MeCN)_2(H_2O)_2](ClO_4)_4\cdot 3MeCN\cdot Et_2O$ (1). Although the some of the atoms in the perchlorate anions have a slightly higher thermal parameters (Ueq) than ideal, they were not split and modeled over two sites, as the higher Ueq values were the most effective way to model these atoms. The half occupancy MeCN was restrained by SAME to be similar to the full occupancy MeCN of solvation. DELU C9 C10 was employed but with default settings had no impact on removing the B alert regarding Ueq of C10 being higher than its neighbours. As Ueq was only 0.08 for that atom it was not pursued further.

$[Ni^{II}_2L^{Et}(MeCN)_4](ClO_4)_4\cdot 1.5MeCN$ (4'). Three of the perchlorate anions are ordered but the fourth has a rotational, 'twirl', disorder about the Cl4-O41 bond. This was modeled by two sets of atoms, Cl42-Cl44:Cl45-Cl47 with 0.5:0.5 occupancy, and restrained by SAME to be similar to a well behaved perchlorate (Cl1-O14).

$[Zn^{II}_2L^{Et}(BF_4)_2](BF_4)_2\cdot 0.3MeCN\cdot 0.4Et_2O$ (6). One of the tetrafluoroborate anions is disordered over two complete sites, B4-F41-F44 and B41-F45-F48, with 0.60:0.40 occupancy. Both parts were restrained by SAME to have a similar geometry to a well behaved anion (B1-F11-F14), and SIMU B41 was used with default esds. A region of overlapping disordered solvent molecules was modelled as two 0.2 occupancy Et_2O molecules and one 0.3 occupancy MeCN. The two Et_2O molecules were restrained using SADI to have similar bond lengths. DFIX and DANG were employed to help restrain the geometry of the 0.3 occupancy MeCN. These disordered solvent molecules were kept isotropic. Two of the carbon atoms of the pyridine ring are split into two parts (C26 and C27) vs (C126 and C127), with 0.5 occupancies, due to a 'flap' type positional disorder of this ring, hinged at N14 and C24. All H atoms are in calculated positions and ride on the attached non-H atom. OMIT 0 0 1 was employed as this reflection was behind the beamstop.

$[Co^{II}_4(L^{Et})_2(F)_4](BF_4)_4\cdot 2.4MeOH$ (9). The hydrogen atom on the methanol oxygen atom was inserted using HFIX 147. Whilst one of the two tetrafluoroborate anions in the asymmetric unit is ordered (B1-F11-F14), the other one is disordered. It was modelled by splitting it into two complete parts, B2-F21-F24 to B21-F25-F28, with 0.8:0.2 occupancy. Both parts were restrained using SAME to be similar to the well behaved B1-F11-F14 ion. The methanol molecule (O60, C60), with 0.2

occupancy, was restrained by SAME to be similar to the full occupancy methanol molecule (O50, C50).

$[Ni^{II}_4(L^{Et})_2(F)_4](BF_4)_4 \cdot 4MeOH$ (10). Both of the methanol molecules were disordered, so were modelled by splitting into two parts (O50, C50: O51, C51) and (O60, C60:O61, C61) with 0.65:0.35 and 0.70:0.30 occupancy, respectively. Both of the BF_4 anions were disordered. One was split into two parts sharing one common F, i.e. B1-F11-F14 and B11-F15-F18 with 0.85:0.15 occupancy, respectively, where EXYZ and EADP commands were used to ensure F11 and F15 had the same coordinates and U values, and B11-F15-F18 was restrained using SAME to have a similar geometry to the well behaved B1:F11-F14 anion. The second BF_4 was modelled by splitting it into two complete, overlapping, parts, B2-F21-F24 and B21-F25-F28 with 0.60:0.40 occupancy, and both parts were restrained using SAME to have a similar geometry to the well behaved B1-F11-F14 anion.

$[Zn^{II}_4(L^{Et})_2(F)_4](BF_4)_4 \cdot 2MeOH \cdot H_2O$ (12). The two disordered oxygen atoms of water, each 0.25 occupancy, were refined isotropically. Both of the BF_4 anions were ordered. The hydrogen atoms on the oxygen atoms of the methanol molecules were inserted using HFIX 147, and that on the oxygen atom of water was found from the electron density map and its coordinates subsequently fixed using the AFIX 01 command after the bond lengths had been improved to 0.85 Å by the HIMP command. The residual Q1 (+0.73) electron density occurs in the same region of space as the two 0.25 occupancy water molecules and their symmetry generated equivalents (Q2 is just +0.58). Note that only one of these four 0.25 occupancy water molecules is present at any one time.

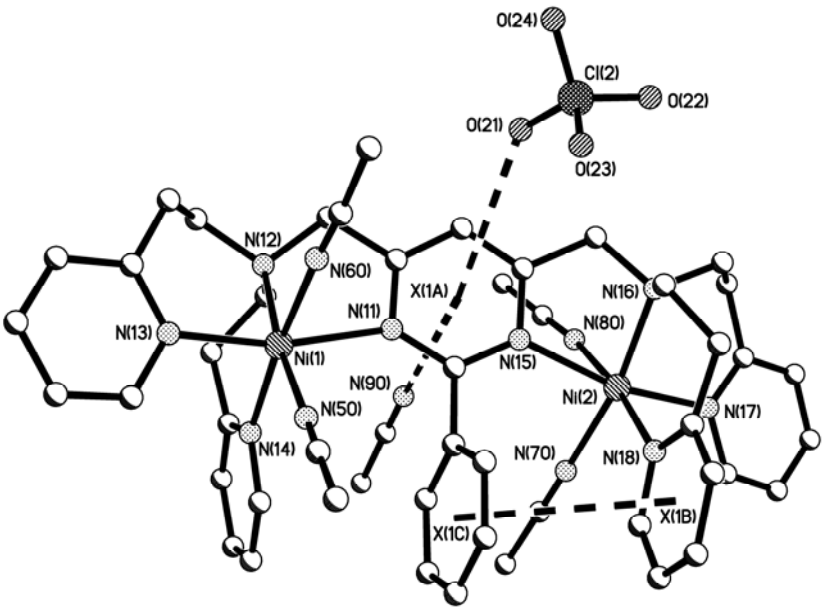

Figure S1: View of the π…π [x(1b)…x(1c) = 3.923 Å], anion…π [O(21)…x(1a) = 3.694 Å] and solvent…π [N(90)…x(1a) = 3.603 Å] interactions in $[Ni^{II}_2L^{Et}(MeCN)_4](ClO_4)_4 \cdot 1.5MeCN$ (4').

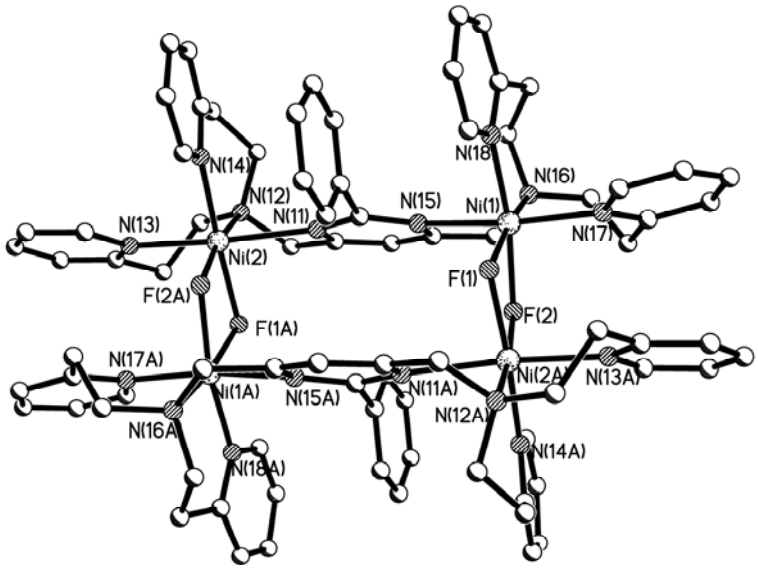

Figure S2: View of the molecular structure of the cation of $[Ni^{II}_4(L^{Et})_2(F)_4](BF_4)_4 \cdot 4MeOH$ (10). Hydrogen atoms, counter ions and solvent molecules have been omitted for clarity. Symmetry operation A = -x+1,-y,-z+1

Table S2: Interatomic distances (Å) and angles (°) around the manganese(II) ions in $[Mn^{II}_2L^{Et}(MeCN)_2(H_2O)_2](ClO_4)_4 \cdot 3MeCN \cdot Et_2O$ (1).

Mn(1)-N(50)	2.206(6)	Mn(1)-N(14)	2.240(6)
Mn(1)-O(40)	2.234(5)	Mn(1)-N(12)	2.289(6)
Mn(1)-N(13)	2.239(6)	Mn(1)-N(11)	2.321(6)
N(50)-Mn(1)-O(40)	82.9(2)	N(13)-Mn(1)-N(12)	88.4(2)
N(50)-Mn(1)-N(13)	89.2(3)	N(14)-Mn(1)-N(12)	91.7(2)
O(40)-Mn(1)-N(13)	87.8(2)	N(50)-Mn(1)-N(11)	106.4(3)
N(50)-Mn(1)-N(14)	94.4(2)	O(40)-Mn(1)-N(11)	79.7(2)
O(40)-Mn(1)-N(14)	175.8(2)	N(13)-Mn(1)-N(11)	158.5(2)
N(13)-Mn(1)-N(14)	95.3(2)	N(14)-Mn(1)-N(11)	98.1(2)
N(50)-Mn(1)-N(12)	173.6(2)	N(12)-Mn(1)-N(11)	74.5(2)
O(40)-Mn(1)-N(12)	91.1(2)		

Table S3: Interatomic distances (Å) and angles (°) around the nickel(II) ions in $[Ni^{II}_2L^{Et}(MeCN)_4](ClO_4)_4 \cdot 1.5MeCN$ (4').

Ni(1)-N(13)	2.062(4)	Ni(2)-N(70)	2.084(4)
Ni(1)-N(50)	2.074(4)	Ni(2)-N(17)	2.086(4)
Ni(1)-N(12)	2.098(4)	Ni(2)-N(16)	2.091(3)
Ni(1)-N(14)	2.123(4)	Ni(2)-N(18)	2.123(4)
Ni(1)-N(11)	2.208(4)	Ni(2)-N(80)	2.188(4)
Ni(1)-N(60)	2.212(4)	Ni(2)-N(15)	2.214(3)
N(13)-Ni(1)-N(50)	90.39(16)	N(70)-Ni(2)-N(17)	92.24(15)
N(13)-Ni(1)-N(12)	92.15(15)	N(70)-Ni(2)-N(16)	169.06(14)
N(50)-Ni(1)-N(12)	170.88(14)	N(17)-Ni(2)-N(16)	93.63(14)
N(13)-Ni(1)-N(14)	92.71(15)	N(70)-Ni(2)-N(18)	93.54(14)
N(50)-Ni(1)-N(14)	92.92(13)	N(17)-Ni(2)-N(18)	92.08(15)
N(12)-Ni(1)-N(14)	95.71(14)	N(16)-Ni(2)-N(18)	95.46(14)
N(13)-Ni(1)-N(11)	166.71(14)	N(70)-Ni(2)-N(80)	79.03(15)
N(50)-Ni(1)-N(11)	97.13(14)	N(17)-Ni(2)-N(80)	89.19(14)
N(12)-Ni(1)-N(11)	78.79(13)	N(16)-Ni(2)-N(80)	91.83(15)
N(14)-Ni(1)-N(11)	97.81(13)	N(18)-Ni(2)-N(80)	172.51(14)
N(13)-Ni(1)-N(60)	88.53(16)	N(70)-Ni(2)-N(15)	95.97(14)
N(50)-Ni(1)-N(60)	79.64(15)	N(17)-Ni(2)-N(15)	166.45(13)
N(12)-Ni(1)-N(60)	91.67(15)	N(16)-Ni(2)-N(15)	76.62(13)
N(14)-Ni(1)-N(60)	172.46(15)	N(18)-Ni(2)-N(15)	98.13(14)
N(11)-Ni(1)-N(60)	82.09(14)	N(80)-Ni(2)-N(15)	81.84(13)

Table S4: Interatomic distances (Å) and angles (°) around the zinc(II) ions in $[Zn^{II}_2L^{Et}(BF_4)_2](BF_4)_2 \cdot 0.3MeCN \cdot 0.4Et_2O$ (6).

Zn(1)-F(34)	2.010(3)	Zn(2)-F(24)	2.017(3)
Zn(1)-N(13)	2.029(4)	Zn(2)-N(17)	2.027(4)
Zn(1)-N(12)	2.101(4)	Zn(2)-N(16)	2.109(4)
Zn(1)-N(14)	2.175(4)	Zn(2)-N(18)	2.133(4)
Zn(1)-N(11)	2.295(4)	Zn(2)-N(15)	2.304(4)
F(34)-Zn(1)-N(13)	108.99(15)	F(24)-Zn(2)-N(17)	106.02(15)
F(34)-Zn(1)-N(12)	149.29(14)	F(24)-Zn(2)-N(16)	149.08(14)
N(13)-Zn(1)-N(12)	101.59(16)	N(17)-Zn(2)-N(16)	103.62(16)
F(34)-Zn(1)-N(14)	88.85(16)	F(24)-Zn(2)-N(18)	92.66(15)
N(13)-Zn(1)-N(14)	96.02(17)	N(17)-Zn(2)-N(18)	98.22(17)
N(12)-Zn(1)-N(14)	90.68(16)	N(16)-Zn(2)-N(18)	91.64(15)
F(34)-Zn(1)-N(11)	95.51(14)	F(24)-Zn(2)-N(15)	89.50(13)
N(13)-Zn(1)-N(11)	98.62(15)	N(17)-Zn(2)-N(15)	100.17(15)
N(12)-Zn(1)-N(11)	76.91(14)	N(16)-Zn(2)-N(15)	76.74(14)
N(14)-Zn(1)-N(11)	162.42(15)	N(18)-Zn(2)-N(15)	160.10(15)

Table S5: Interatomic distances (Å) and angles (°) around the cobalt(II) ions in $[Co^{II}_4(L^{Et})_2(F)_4](BF_4)_4 \cdot 2.4MeOH$ (9)

Co(1)-F(2)	1.9922(12)	Co(2)-F(2a)	2.0528(12)
Co(1)-F(1)	2.0954(12)	Co(2)-F(1a)	2.0545(12)
Co(1)-N(14)	2.1376(18)	Co(2)-N(18)	2.1335(18)
Co(1)-N(12)	2.1614(18)	Co(2)-N(17)	2.1502(19)
Co(1)-N(13)	2.1976(18)	Co(2)-N(16)	2.1767(18)
Co(1)-N(11)	2.3904(17)	Co(2)-N(15)	2.3160(17)
F(2)-Co(1)-F(1)	76.70(5)	F(2a)-Co(2)-F(1a)	76.31(5)
F(2)-Co(1)-N(14)	92.76(6)	F(2a)-Co(2)-N(18)	172.57(6)
F(1)-Co(1)-N(14)	169.20(6)	F(1a)-Co(2)-N(18)	97.28(6)
F(2)-Co(1)-N(12)	169.82(6)	F(2a)-Co(2)-N(17)	97.05(6)
F(1)-Co(1)-N(12)	94.31(6)	F(1a)-Co(2)-N(17)	89.35(6)
N(14)-Co(1)-N(12)	95.99(7)	N(18)-Co(2)-N(17)	86.51(7)
F(2)-Co(1)-N(13)	97.38(6)	F(2a)-Co(2)-N(16)	91.29(6)
F(1)-Co(1)-N(13)	97.25(6)	F(1a)-Co(2)-N(16)	167.20(6)
N(14)-Co(1)-N(13)	86.33(7)	N(18)-Co(2)-N(16)	95.29(7)
N(12)-Co(1)-N(13)	88.39(7)	N(17)-Co(2)-N(16)	89.05(7)
F(2)-Co(1)-N(11)	99.88(6)	F(2a)-Co(2)-N(15)	87.59(6)
F(1)-Co(1)-N(11)	86.07(5)	F(1a)-Co(2)-N(15)	106.13(6)
N(14)-Co(1)-N(11)	93.54(6)	N(18)-Co(2)-N(15)	90.66(6)
N(12)-Co(1)-N(11)	74.43(6)	N(17)-Co(2)-N(15)	164.50(7)
N(13)-Co(1)-N(11)	162.72(7)	N(16)-Co(2)-N(15)	76.03(6)

Symmetry operation used to generate equivalent atoms: a = -x+3/2,-y+1/2,-z

Table S6: Interatomic distances (Å) and angles (°) around the nickel(II) ions in $[Ni^{II}_4(L^{Et})_2(F)_4](BF_4)_4 \cdot 4MeOH$ (10)

Ni(1)-F(1)	2.0262(9)	Ni(2)-F(2a)	2.0049(9)
Ni(1)-F(2)	2.0358(9)	Ni(2)-F(1a)	2.0416(9)
Ni(1)-N(18)	2.0691(14)	Ni(2)-N(14)	2.0780(14)
Ni(1)-N(17)	2.1010(13)	Ni(2)-N(13)	2.1106(13)
Ni(1)-N(16)	2.1353(14)	Ni(2)-N(12)	2.1242(14)
Ni(1)-N(15)	2.3083(13)	Ni(2)-N(11)	2.2841(12)
F(1)-Ni(1)-F(2)	76.01(3)	F(2a)-Ni(2)-F(1a)	76.35(3)
F(1)-Ni(1)-N(18)	94.91(5)	F(2a)-Ni(2)-N(14)	94.68(5)
F(2)-Ni(1)-N(18)	169.03(5)	F(1a)-Ni(2)-N(14)	169.72(5)
F(1)-Ni(1)-N(17)	90.04(4)	F(2a)-Ni(2)-N(13)	90.99(4)
F(2)-Ni(1)-N(17)	97.41(4)	F(1a)-Ni(2)-N(13)	96.90(4)
N(18)-Ni(1)-N(17)	88.62(5)	N(14)-Ni(2)-N(13)	88.16(5)
F(1)-Ni(1)-N(16)	168.68(5)	F(2a)-Ni(2)-N(12)	169.36(5)
F(2)-Ni(1)-N(16)	92.68(5)	F(1a)-Ni(2)-N(12)	93.06(5)
N(18)-Ni(1)-N(16)	96.27(6)	N(14)-Ni(2)-N(12)	95.78(6)
N(17)-Ni(1)-N(16)	91.92(5)	N(13)-Ni(2)-N(12)	91.32(5)
F(1)-Ni(1)-N(15)	102.87(4)	F(2a)-Ni(2)-N(11)	101.64(4)
F(2)-Ni(1)-N(15)	85.46(4)	F(1a)-Ni(2)-N(11)	83.85(4)
N(18)-Ni(1)-N(15)	90.69(5)	N(14)-Ni(2)-N(11)	93.22(5)
N(17)-Ni(1)-N(15)	167.08(5)	N(13)-Ni(2)-N(11)	167.12(5)
N(16)-Ni(1)-N(15)	75.33(5)	N(12)-Ni(2)-N(11)	75.80(5)

Symmetry operation used to generate equivalent atoms: a = -x+1,-y,-z+1

Table S7: Interatomic distances (Å) and angles (°) around the zinc(II) ions in $[Zn^{II}_4(L^{Et})_2(F)_4](BF_4)_4 \cdot 2MeOH \cdot H_2O$ (12)

Zn(1)-F(1)	1.9860(15)	Zn(2)-F(2a)	1.9485(15)
Zn(1)-F(2)	2.0581(14)	Zn(2)-N(17)	2.064(2)
Zn(1)-N(13)	2.085(2)	Zn(2)-N(16)	2.097(2)
Zn(1)-N(12)	2.115(2)	Zn(2)-F(1a)	2.1027(14)
Zn(1)-N(14)	2.123(2)	Zn(2)-N(18)	2.139(2)
Zn(1)···N(11)	2.889(2)	Zn(1) ···N(15)	3.015(2)
F(1)-Zn(1)-F(2)	76.30(6)	F(2a)-Zn(2)-N(17)	105.57(8)
F(1)-Zn(1)-N(13)	101.20(7)	F(2a)-Zn(2)-N(16)	154.24(7)
F(2)-Zn(1)-N(13)	94.92(7)	N(17)-Zn(2)-N(16)	97.96(8)
F(1)-Zn(1)-N(12)	158.54(7)	F(2a)-Zn(2)-F(1a)	76.06(6)
F(2)-Zn(1)-N(12)	90.26(7)	N(17)-Zn(2)-F(1a)	89.75(7)
N(13)-Zn(1)-N(12)	96.50(8)	N(16)-Zn(2)-F(1a)	93.97(7)
F(1)-Zn(1)-N(14)	93.95(7)	F(2a)-Zn(2)-N(18)	90.04(7)
F(2)-Zn(1)-N(14)	166.54(7)	N(17)-Zn(2)-N(18)	98.62(8)
N(13)-Zn(1)-N(14)	96.09(8)	N(16)-Zn(2)-N(18)	96.75(8)
N(12)-Zn(1)-N(14)	96.15(8)	F(1a)-Zn(2)-N(18)	165.33(7)
N(11)-Zn(1)-N(12)	69.11(8)	N(15)-Zn(2)-N(16)	66.30(8)
N(11)-Zn(1)-F(1)	92.09(6)	N(11)-Zn(2)-F(1a)	84.78(6)
N(11)-Zn(1)-F(2)	81.43(6)	N(11)-Zn(2)-F(2a)	88.91(6)
(11)-Zn(1)-N(13)	165.01(8)	N(15)-Zn(2)-N(17)	162.83(8)
(11)-Zn(1)-N(13)	89.81(8)	N(15)-Zn(2)-N(17)	90.39(8)

Symmetry operation used to generate equivalent atoms: a = x, y-1, z

Table S8: Comparison of the angles of intersection (º) of the mean planes through various rings in the dinuclear complexes.

Complex	Pym^Ph[a]	Pym^Py[b] [mean]	Pym^Py[c] [mean]	Py^Py[d] [mean]
1	90.0(1)	15.1(3)	85.3(2)	86.5(2)
4'	71.2(1)	26.9(1), 30.7(1) [28.8]	74.4(1), 76.8(1) [75.6]	75.7(2), 77.0(1) [76.4]
6	77.1(1)	13.6(5), 21.8(3) [17.7]	73.2(2)[e], 74.4(2) [73.8]	84.6(2), 86.2(2) [85.4]

[a] Angle between the phenyl and pyrimidine mean planes. [b] Angle between the pyridine rings that are approximately parallel to the pyrimidine plane ('axial'). [c] Angle between the pyrimidine and the pyridine rings that are approximately at right angles to the pyrimidine planes ('equatorial'). [d] Angle between the two pyridine rings on each binding pocket.
[e] The pyridine rings in this complex occupied the apical position relative to the square base.

Table S9 : Comparison of the angles of intersection (°) of various mean planes in the tetranuclear complexes

Complex	Pym/ph[a]	Pym/py[b]	Pym/py[c]	Ph/py[d]	Ph/py[e]	(Py/py)[f]
9	69.66(7)	8.04(1), 16.68(1)	70.49(6)-87.93(7)	69.56(7)-80.32(7)	1.18(15), 27.74(9)	70.26(7)-74.46(8)
10	87.48(5)	3.54(11), 10.89(11)	85.32(5)-89.62(5)	82.24(5)-87.48(5)	6.02(12), 7.07(12)	79.79(5)-84.38(5)
12	3.83(11)	8.04(12), 12.77(12)	80.47(8)-81.46(8)	7.81(13)-11.36(13)	83.07(9), 78.96(8)	75.51(9)-88.22(8)

[a] Angle between the phenyl and pyrimidine mean planes on the same ligand strand. [b] Angle between the pyridines parallel to the pyrimidine plane on the same ligand strand. [c] Angle between the pyridine almost normal to the pyrimidine plane on the same ligand strand. [d] Angle between the phenyl ring and the pyridines (parallel to the pyrimidine plane) from the same ligand strand.[e] Angle between the pyridine rings (normal to the pyrimidine plane) and the phenyl ring from the same ligand strand.[f] Angle between two same side pyridines on the same ligand strand.

Table S10: Hydrogen bonds present in $[Mn^{II}_2L^{Et}(MeCN)_2(H_2O)_2](ClO_4)_4\cdot 3MeCN\cdot Et_2O$(1) [Å and °].

D-H...A	d(D-H)	d(H...A)	d(D...A)	<(DHA)
O(40)-H(40X)...O(24)	0.83	2.21	2.875(10)	137.1
O(40)-H(40Y)...O(34)	0.80	2.25	2.880(30)	136.4

Table S11: Hydrogen bonds present in $[Co^{II}_4(L^{Et})_2(F)_4](BF_4)_4\cdot 2.4MeOH$ [Å and °].

D-H...A	d(D-H)	d(H...A)	d(D...A)	<(DHA)
O(50)-H(50X)...F(21)	0.84	2.10	2.902(7)	158.7
O(50)-H(50X)...F(23)	0.84	2.52	3.123(4)	129.4
O(50)-H(50X)...F(25)	0.84	2.20	3.02(3)	165.4
O(60)-H(60X)...F(24)	0.84	2.32	2.963(4)	133.3

Table S12: Hydrogen bonds present in $[Ni^{II}_4(L^{Et})_2(F)_4](BF_4)_4 \cdot 4MeOH$ [Å and °].

D-H...A	d(D-H)	d(H...A)	d(D...A)	<(DHA)
O(50)-H(50)...O(60)	0.84	1.96	2.780(4)	165.1
O(60)-H(60)...F(22)	0.84	1.98	2.795(4)	164.3
O(51)-H(51)...F(18)	0.84	1.89	2.730(14)	175.6
O(61)-H(61)...F(26)	0.84	2.01	2.805(9)	157.6

Table S13: Hydrogen bonds present in $[Zn^{II}_4(L^{Et})_2(F)_4](BF_4)_4 \cdot 2MeOH \cdot H_2O$ [Å and °].

D-H...A	d(D-H)	d(H...A)	d(D...A)	<(DHA)
O(50)-H(50X)...F(21)	0.84	1.95	2.778(3)	166.9
O(60)-H(60X)...F(23)	0.85	2.11	2.945(10)	169.2

Table S14: Comparison of distances (Å) and offset angles (°) for the various pair of rings in the tetranuclear complexes 9, 10 and 12 showing the presence of π-π intramolecular interaction.

Complex	$[Co^{II}_4(L^{Et})_2(F)_4](BF_4)_4$ ·2.4MeOH (**9**)	$[Ni^{II}_4(L^{Et})_2(F)_4](BF_4)_4$ ·4MeOH (**10**)	$[Zn^{II}_4(L^{Et})_2(F)_4](BF_4)_4$ ·2MeOH·H_2O (**12**)
Pyrimidine to phenyl ring[a]			
Centroid to centroid (Å)	-	-	3.542
Mean plane to centroid (Å)	-	-	3.287
Offset angle (°)	-	-	21.9
Pyridine ring pairs[b]			
Centroid to centroid (Å)	3.479	3.432	3.608
Mean plane to centroid (Å)	3.423	3.371	3.227
Offset angle (°)	10.3	10.8	26.6
Pyridine to phenyl ring[c]			
Centroid to centroid (Å)	3.938 - 4.250	3.639 - 3.645	-
Mean plane to centroid (Å)	2.731 - 3.737	3.127 - 3.104	-
Offset angle (°)	18.4 - 46.1	30.8 - 31.6	-

[a] Between pyrimidine and phenyl rings of parallel ligands.[b] Between pyridine rings (parallel to the pyrimidine plane on the same ligand) facing each other between the parallel ligands. [c] Between the pyridine rings (almost normal to the pyrimidine plane on the same ligand) and the phenyl ring.

Table S15: Least square refinement data for $[Co^{II}_4(L^{Et})_2(F)_4](BF_4)_4 \cdot 2.4MeOH$ (9), $[Ni^{II}_4(L^{Et})_2(F)_4](BF_4)_4 \cdot 4MeOH$ (10) and $[Zn^{II}_4(L^{Et})_2(F)_4](BF_4)_4 \cdot 2MeOH \cdot H_2O$ (12), varying X from O to F.

Complex	X	R1 (%)	wR2 (%)	Ueq (M)	Ueq (N)	Ueq (O)	Ueq (F)
9, Cobalt	O	4.19	11.3	0.019	0.021	0.010	-
	F	3.75	9.94	0.019	-	-	0.023
10, Nickel	O	3.37	9.23	0.015	0.016	0.005	-
	F	2.71	6.99	0.016	0.016	-	0.016
12, Zinc	O	4.05	10.9	0.013	0.016	0.002	-
	F	3.64	9.65	0.013	0.016	-	0.015

Electrochemical studies

Cyclic voltammograms (CV) for the dinuclear complexes **1-6** have been recorded as 1 mM dry acetonitrile/0.1M Bu_4PF_6 solutions and were referenced to 0.01molL^{-1} $AgNO_3$/Ag. As a further reference check, ferrocene was added at the conclusion of each experiment: The Fc/Fc^+ couple consistently occurred at $E_{1/2}$ = + 0.06 ± 0.01V with ΔE = 0.08 V in this cell system.

The CV of dizinc complex **6** was investigated in order to study the electrochemical processes of $\mathbf{L^{Et}}$ since the coordinated zinc(II) ions are not expected to undergo reduction or oxidation in the potential range accessible in acetonitrile. The CV shows one high-current irreversible oxidation process at +1.88 V and an irreversible reduction at -1.20 V, both of which are expected to be ligand centered (Figure S3).

The CV of the dicopper(II) complex **5** (+0.10 → -2.00 → +2.00 → 0.10 V) reveals irreversible reductions at E_{pc} = -1.34 and -1.14 V, a quasi-reversible reduction at E_{pc} = -0.03 V and two broad irreversible oxidation waves at *ca*. +0.80 and +1.00 V (Figure S3). In the initial scan range study these latter waves were overlapping, but they separated out into two peaks when the scan was reversed earlier, at -1.50 V (i.e. +0.10 V→ -1.50→ +2.00 → +0.10 V) (Figure S4b). There is also a cathodic wave at -0.90 V which is related to the stripping wave (of metallic copper off the electrode surface) at -0.54 V (Figure S4c). The cathodic peak at -0.03 V has an associated anodic peak at +0.26 V. A scan rate study of this process, with a midwave potential (E_m) approximately equal to +0.11 V (ΔE = 150 mV), run from -0.50 to +0.50 to -0.50 V is best described as quasi-reversible (Figure S5). This reduction process is believed to be metal based. Bulk electrolysis conducted at -0.30 V resulted in the transfer of 1.46 electron equivalents. The UV-Vis spectrum performed after the coulometry did not show the d-d absorption maxima at 625 nm and 925 nm, instead it featured a shoulder at approximately 420 nm, consistent with the copper(II) centers having been reduced to copper(I) (Figure S6).[1] Presumably the absence of two well resolved consecutive metal based reductions is a result of very weak electrochemical communication between the two copper(II) centers. The potential seen for **5** is more positive than in $[Cu^{II}_2\mathbf{L^2}Cl_2][ClO_4]_2{\cdot}4CH_3CN$, reported by Oshio and coworkers, indicating that $\mathbf{L^{Et}}$ stabilizes copper(I) better than the related pyrazine based ligand $\mathbf{L^2}$ does.[2]

The CV of the dinickel complex **4** revealed two irreversible reductions at E_{pc} = -1.30 and -1.81 V and an irreversible oxidation at E_{pa} = +1.11 V (Figure S3). The irreversible nature of the reduction waves was confirmed by a scan rate study (0.00 to -2.00 to 0.00 V, Figure S7). By comparison with **6** the reduction at E_{pc} = -1.30 V is probably ligand based while the irreversible oxidation at +1.11 V is probably metal based. The reduction at E_{pc} = -1.81 V is likely also to be ligand based.[2-4]

The CV of the dicobalt complex **3** revealed irreversible reductions at E_{pc} = -1.32 and -1.77 V and an irreversible oxidation at +1.94 V (Figure S3). The reduction at E_{pc} = -1.77 V appears to have an associated wave at -1.65 V: a scan rate study run from -0.50 to -2.00 and back to -0.50 V shows it to be irreversible (Figure S8). These reductions are similar to the ligand-centred processes seen in dinickel(II) complex **4**, although while the first reduction occurs at almost the same potential, the second reduction occurs at a less negative potential.

The CV of the diiron complex **2** revealed two irreversible oxidations, at +1.48 V and +1.70 V, and three irreversible reductions, at -1.24, -1.60 and -1.80 V (Figure S3). By comparison with the dizinc(II) **6** and the literature reports[2, 4] the three reduction processes are likely to be ligand centered while the oxidation processes at E_{pa} = +1.48 and +1.70 V may be metal based.

The CV of dimanganese complex **1** showed an irreversible oxidation at E_{pa} = +1.75 V and two irreversible reductions at E_{pc} = -0.48 (very weak) and -1.18 V (Figure S3). When the scan was run from 0.00 to only +1.00 then back to -2.00 and back to 0.00 V, the cathodic peak at -1.18 V is not seen (Figure S9). This indicates that the cathodic peak at -1.18 V is associated with the oxidation process at +1.75 V; presumably the complex is irreversibly oxidized, forming a new species that can be reduced at -1.18 V. These redox processes are fairly similar to those seen for **6**, so are likely also predominantly ligand centered.

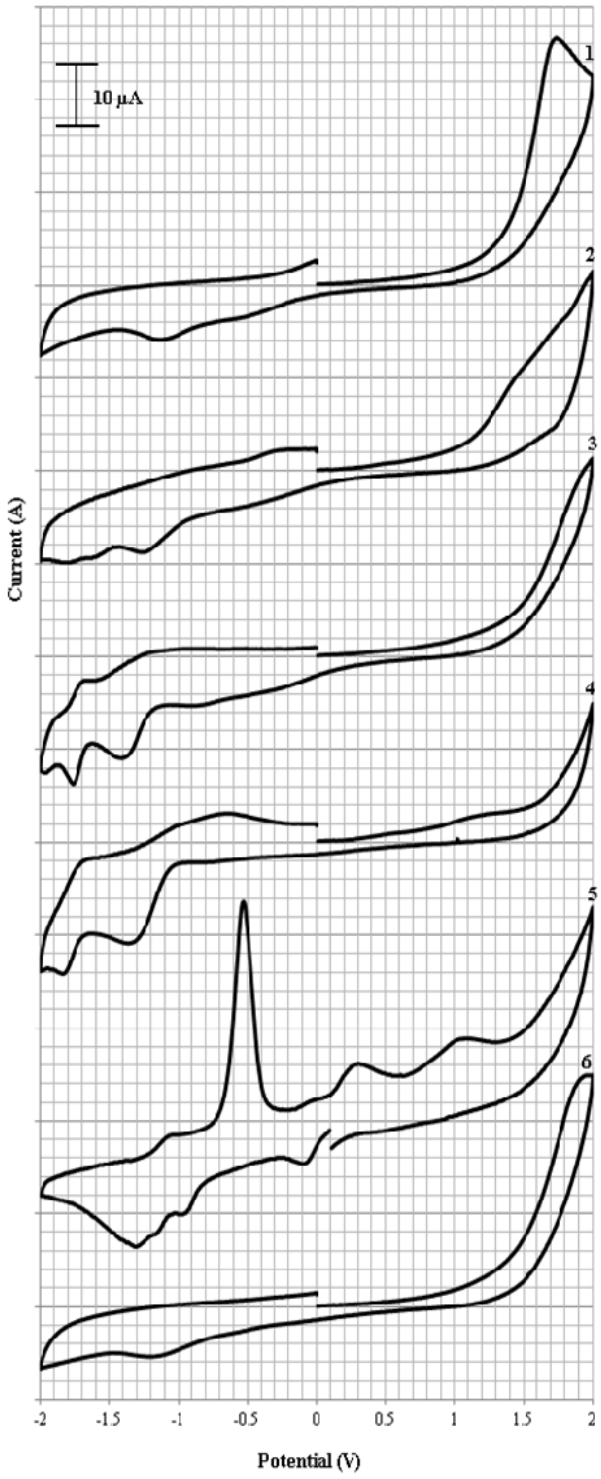

Figure S3: Cyclic voltammograms of dinuclear complexes, from top to bottom: 1 (Mn), 2 (Fe), 3 (Co), 4 (Ni), 5 (Cu) 6 (Zn) run as 1 mmol L^{-1} acetonitrile solutions at 200 mV/s versus 0.01 M $AgNO_3$/Ag. For all but 5 (Cu), the scan was run to positive potential first.

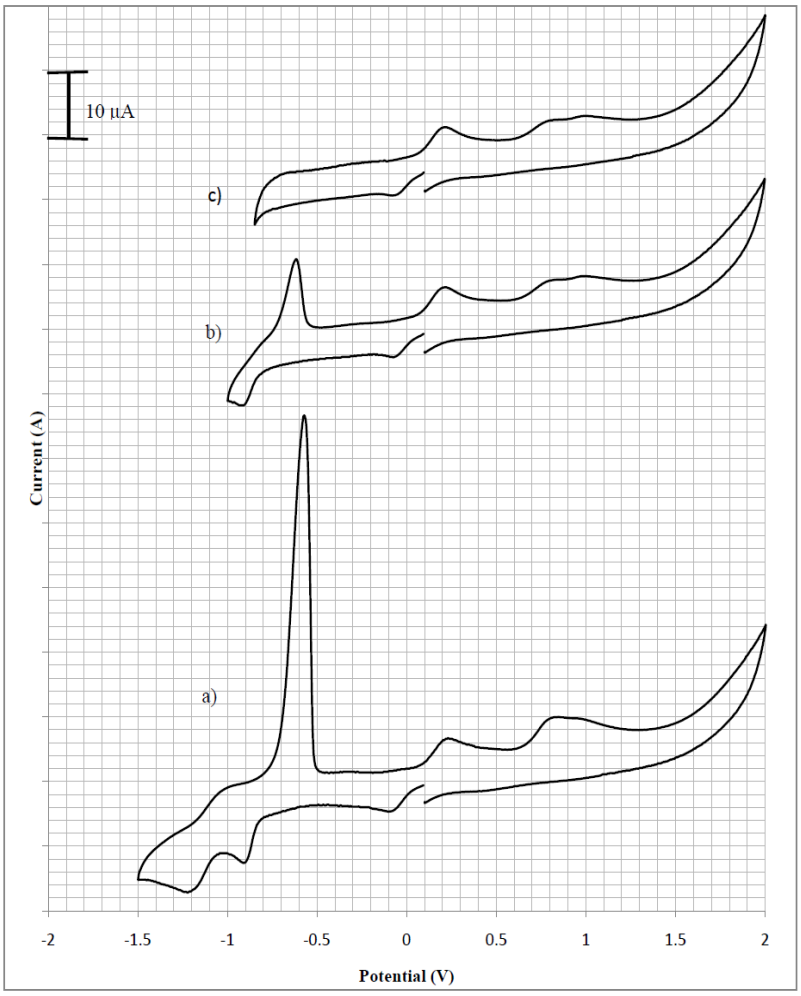

Figure S4: Cyclic voltammograms for $Cu^{II}_2L^{Et}(BF_4)_4$·MeCN (5), run from a) 0.10 to -1.50 to +2.00 to 0.10 V , b) 0.10 to -1.00 to +2.00 to 0.10 V and c) 0.10 to -0.85 to +2.00 to 0.10 V, at 200 mV/s in acetonitrile versus 0.01 M $AgNO_3$/Ag.

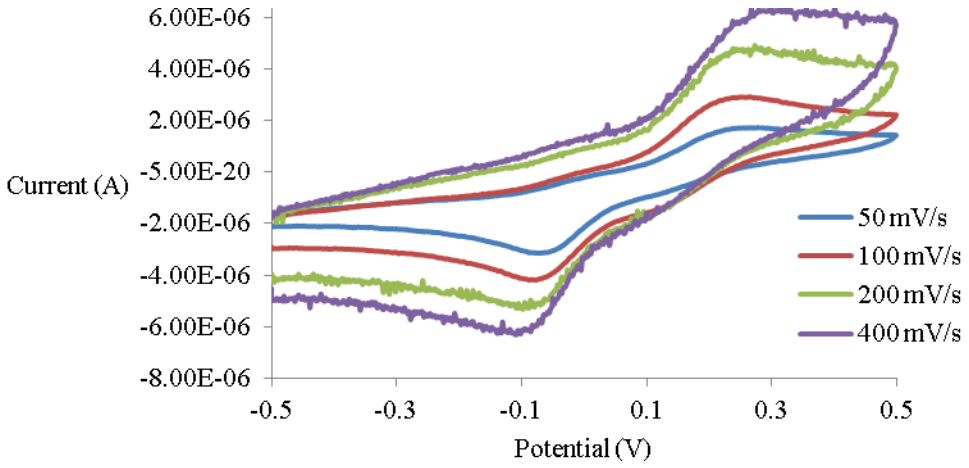

Figure S5: Scan rate study of $Cu^{II}_2L^{Et}(BF_4)_4$·MeCN (5), run from -0.50 to +0.50 to -0.50 V, in acetonitrile vs $AgNO_3$/Ag.

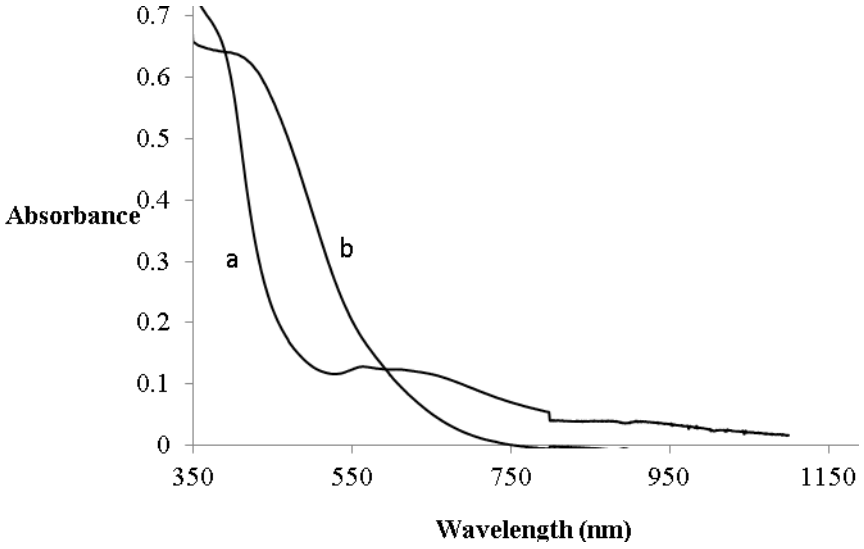

Figure S6: UV-Vis spectra for $Cu^{II}_2L^{Et}(BF_4)_4$·MeCN (5) before (a) and after (b) coulometry, at -0.30 V versus 0.01 $AgNO_3$/Ag, which transferred 1.46 electron equivalents.

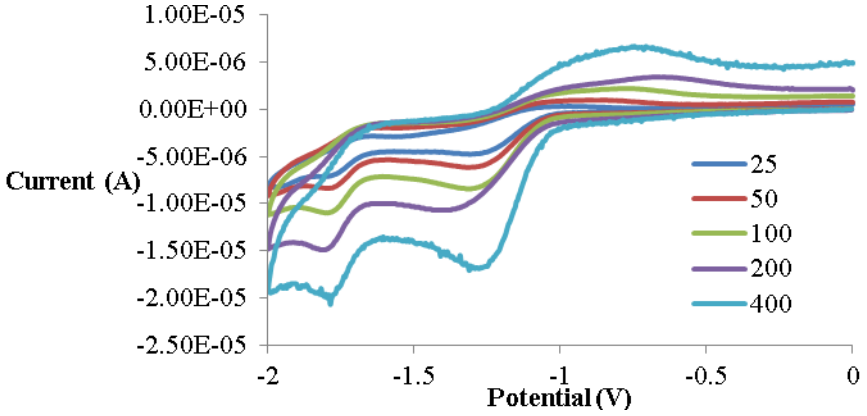

Figure S7: Scan rate study for $Ni^{II}_2L^{Et}(H_2O)_4(BF_4)_4$ (4), run from 0.00 to -2.00 and back to 0.00 V, in acetonitrile vs $AgNO_3$/Ag .

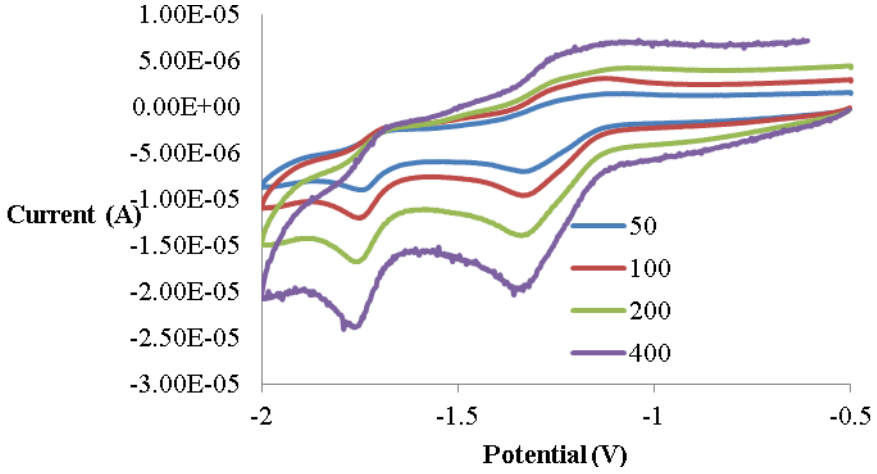

Figure S8: Scan rate study for $Co^{II}_2L^{Et}(H_2O)_3(MeCN)_2(BF_4)_4$ (3), run from -0.50 to -2.00 and back to - 0.50 V, run at 200 mV/s in acetonitrile vs $AgNO_3$/Ag .

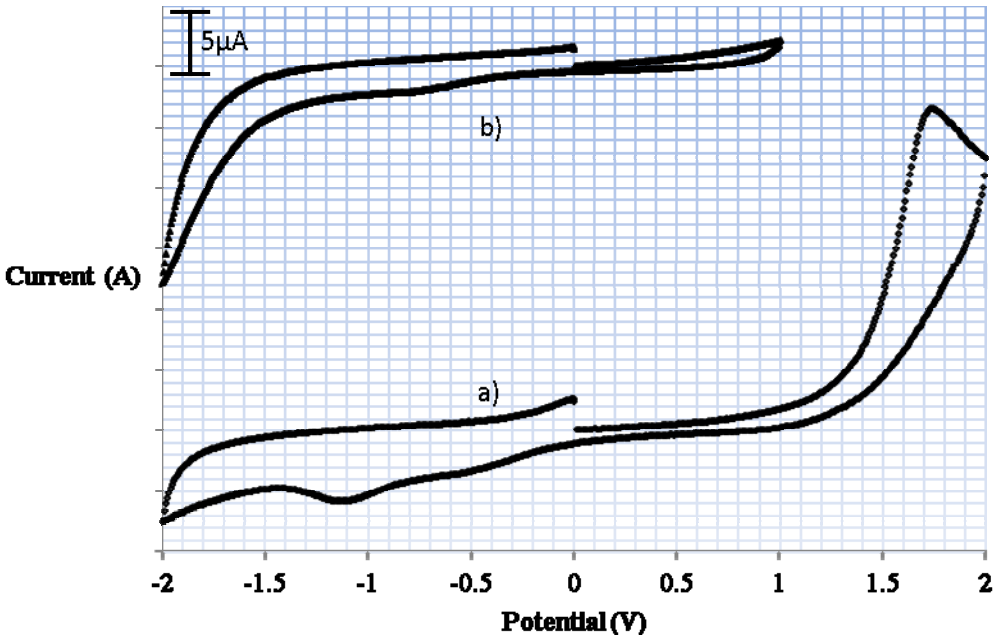

Figure S9: Cyclic voltammograms for $Mn^{II}_2L^{Et}(H_2O)_3(MeCN)(ClO_4)_4$ (1), run from a) 0.00 to +2.00 to -2.00 to 0.00 V b) 0.00 to +1.00 to -2.00 to 0.00 V, at 200 mV/s in acetonitrile versus 0.01 M $AgNO_3$/Ag.

Magnetic studies

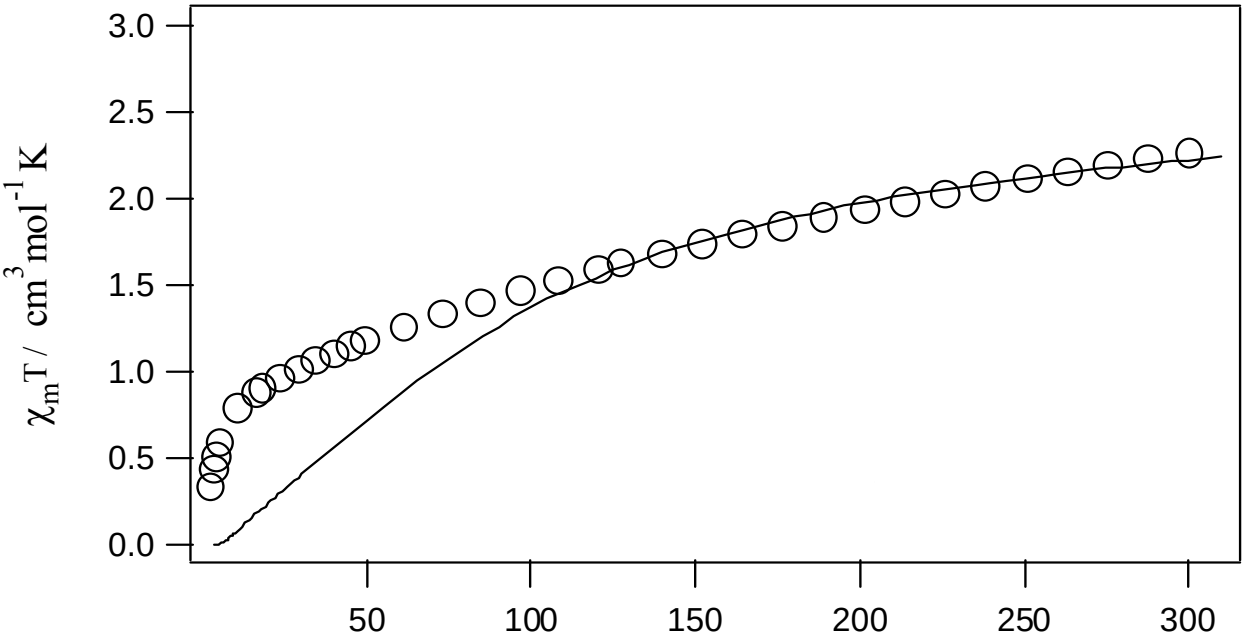

Figure S10: Plot of $\chi_M T$, per Fe, versus temperature for $[Fe^{II}_2L^{Et}(H_2O)_4](BF_4)_4$ (2). The solid line represents the calculated plot.

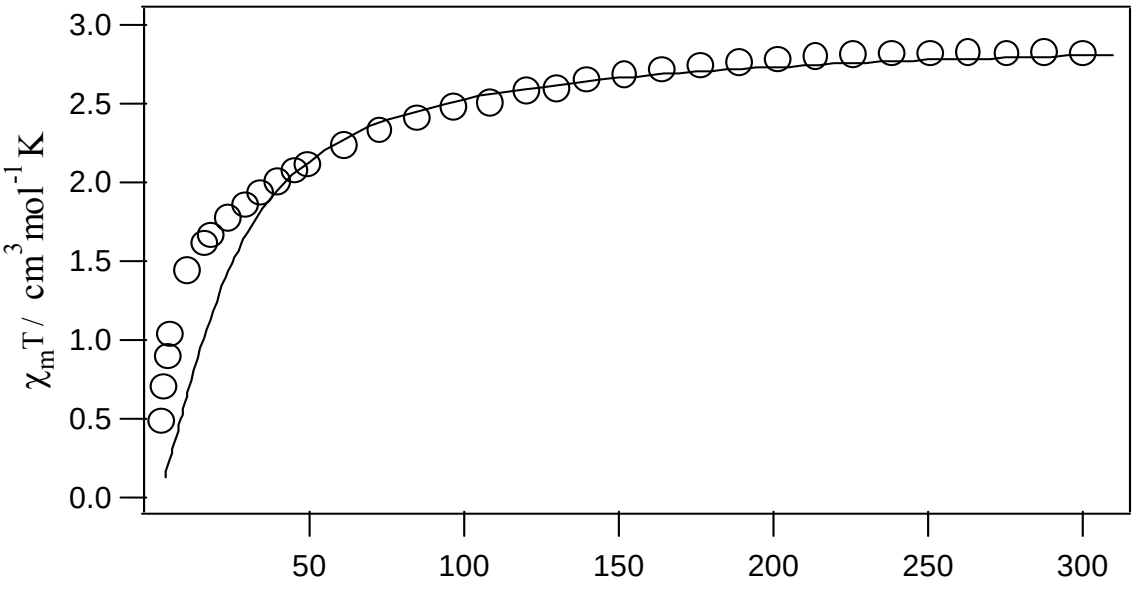

Figure S11: Plot of $\chi_m T$, per Co, versus temperature for $Co^{II}_2L^{Et}(H_2O)_3(MeCN)_2(BF_4)_4$ (3). The solid line corresponds to the best fit

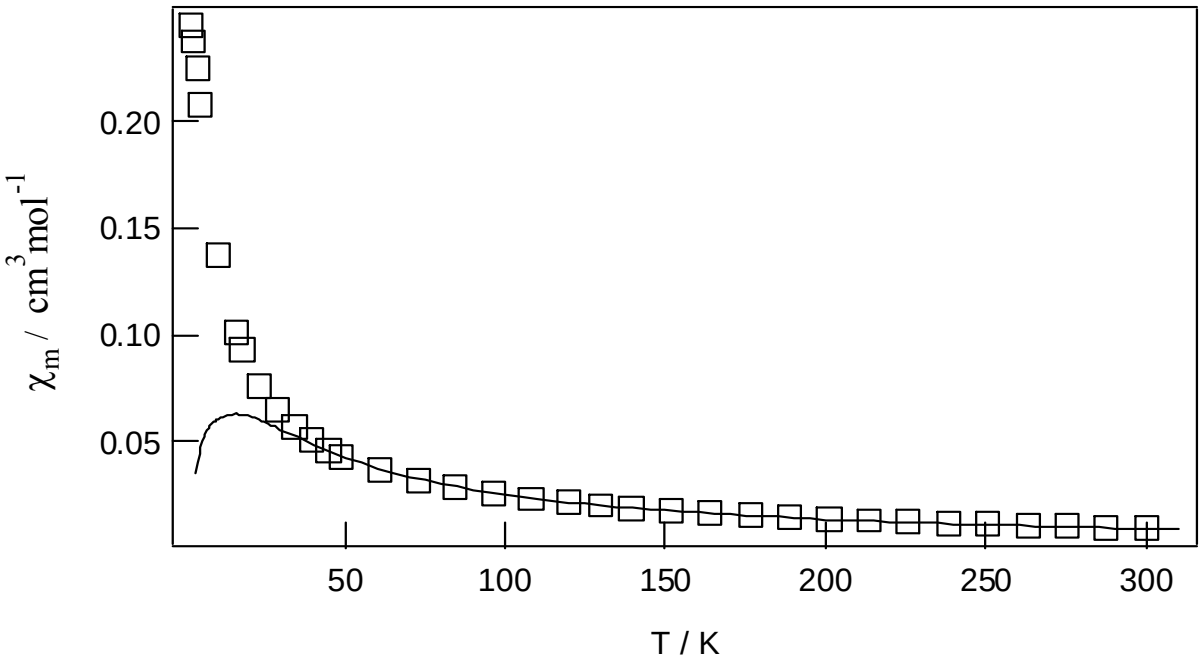

Figure S12: Plot of χ_M, per Co, versus temperature for $Co^{II}_2L^{Et}(H_2O)_3(MeCN)_2(BF_4)_4$ (3). The solid line is the calculated plot.

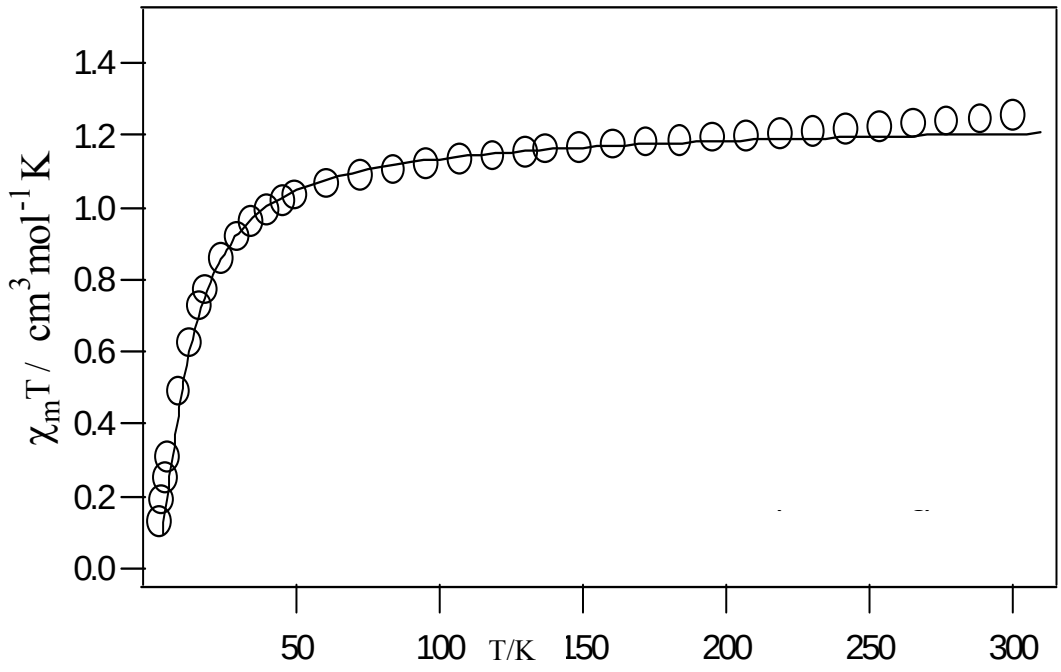

Figure S13: Plot of χ_mT, per Ni, versus temperature for $[Ni^{II}_2L^{Et}(H_2O)_4](BF_4)_4$ (4). The solid line corresponds to the best fit.

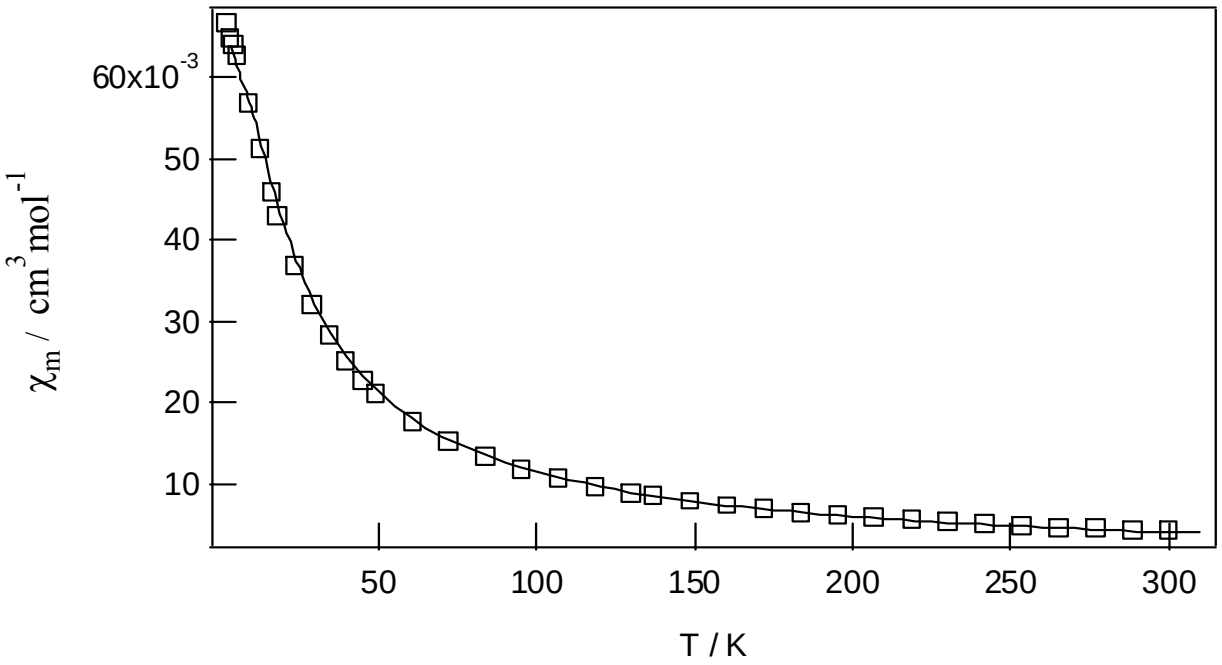

Figure S14: Plot of χ_M, per Ni_2, versus temperature for $[Ni^{II}_2L^{Et}(H_2O)_4](BF_4)_4$ (4). The solid line is the calculated plot.

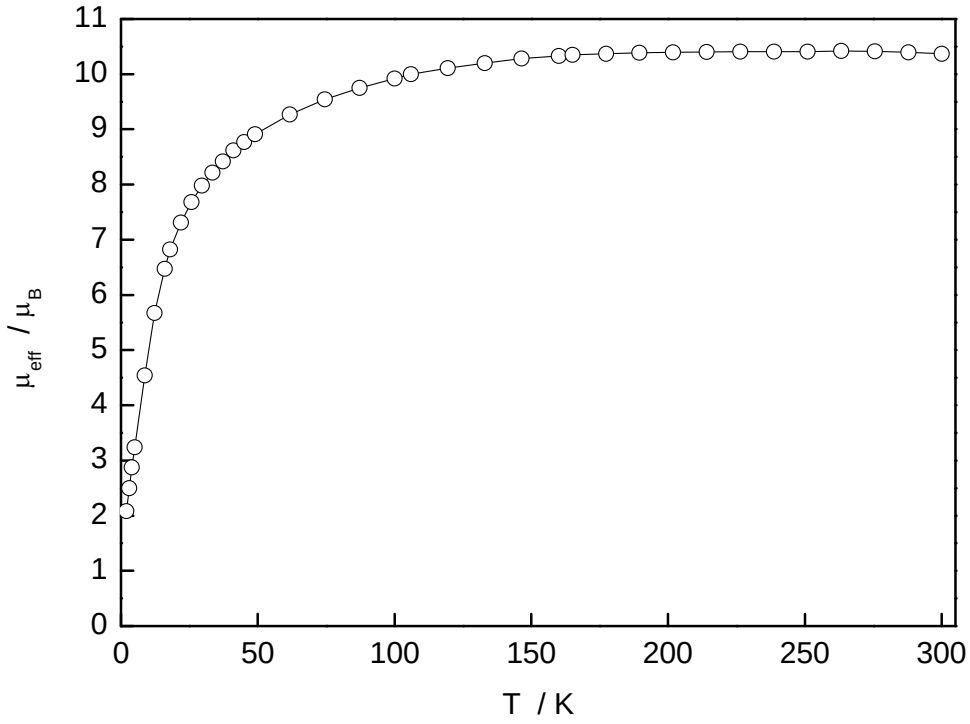

Figure S15: Plot of μ_{eff} per Co_4, versus temperature for $[Co^{II}_4(L^{Et})_2(F)_4](BF_4)_4 \cdot 3H_2O$ (9) in a field of 1 Tesla (10,000 Oe). The solid line just joins the points.

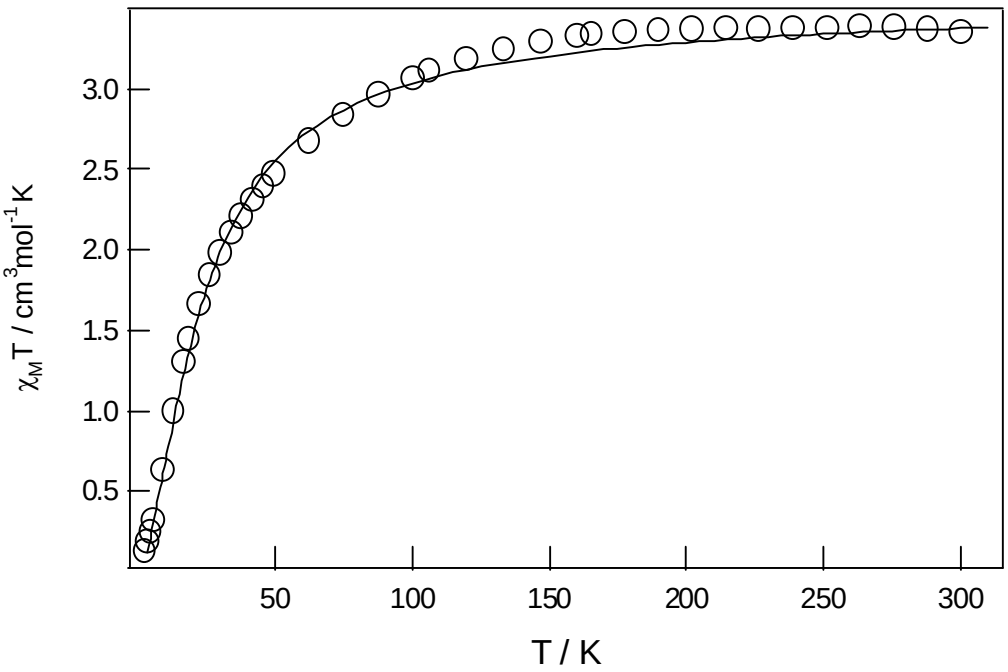

Figure S16: Plot of $\chi_M T$, per Co, versus temperature for $[Co^{II}_4(L^{Et})_2(F)_4](BF_4)_4 \cdot 3H_2O$ (9) in a field of 1 Tesla (10,000 Oe). The solid line is the calculated plot

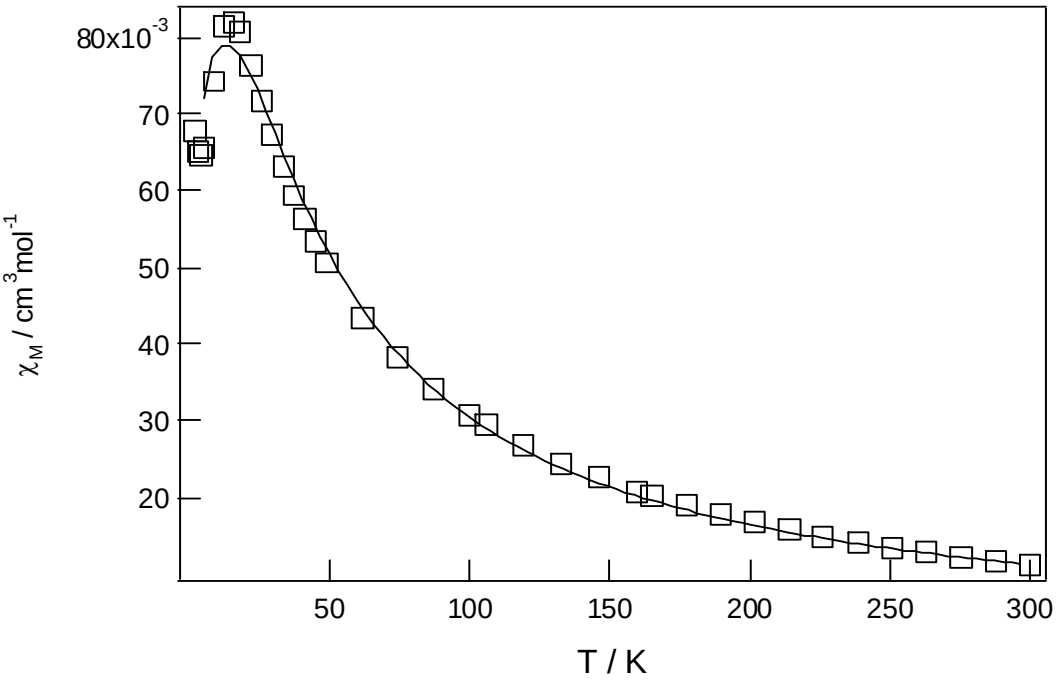

Figure S17: Plot of χ_M, per Co, versus temperature for $[Co^{II}_4(L^{Et})_2(F)_4](BF_4)_4] \cdot 3H_2O$ (9) measured in a field of 1 Tesla (10,000 Oe). The solid line is the calculated plot.

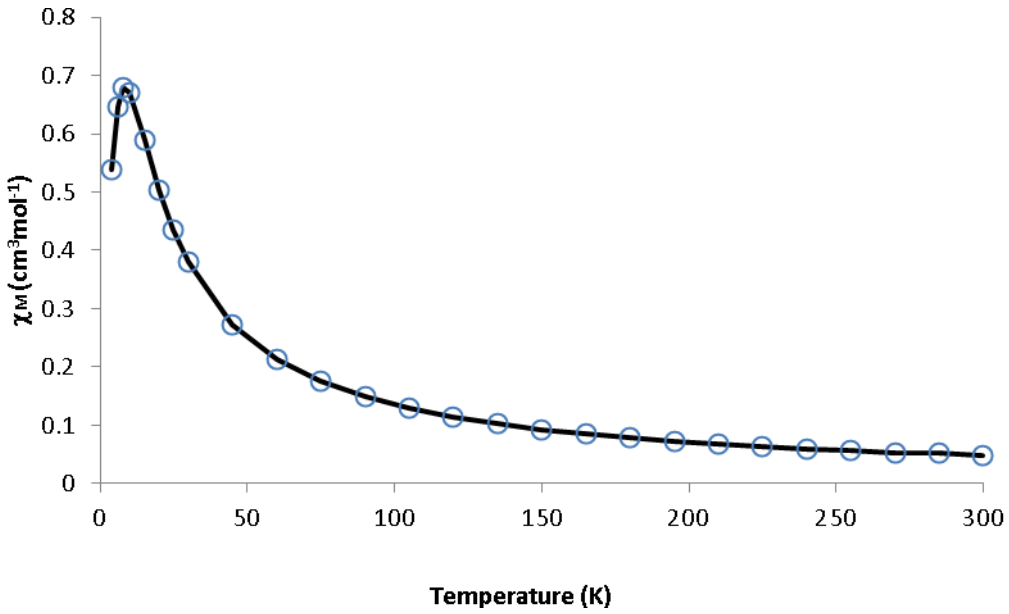

Figure S18: Plot of χ_M, per Fe, versus temperature for $[Fe^{II}_4(L^{Et})_2(F)_4](BF_4)_4 \cdot {}^5/_2H_2O$ (8) measured in a field of 1 Tesla (10,000 Oe). The solid line is the calculated plot.

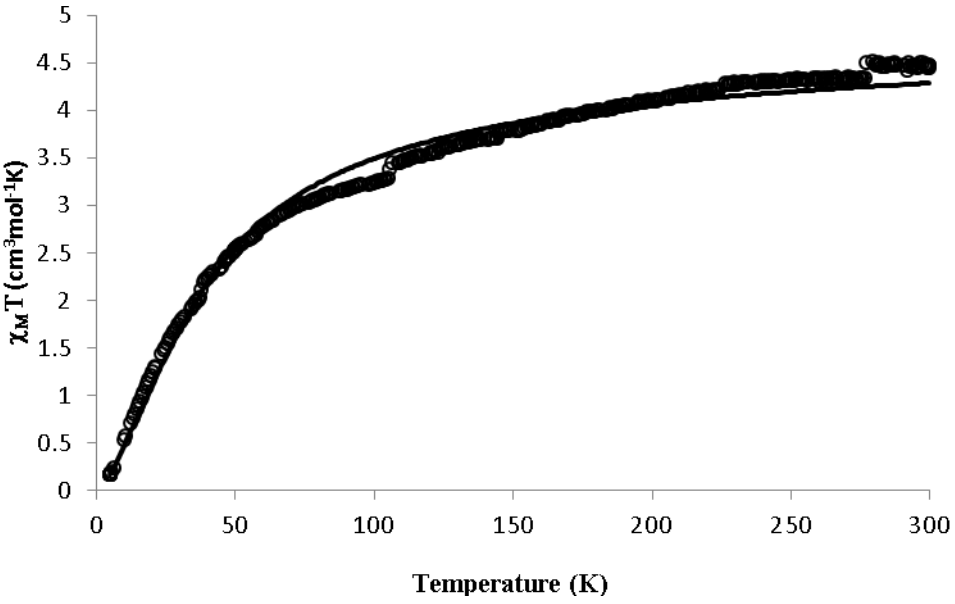

Figure S19: Plot of $\chi_M T$, per Ni_4, versus temperature for $[Ni^{II}_4(L^{Et})_2(F)_4](BF_4)_4 \cdot 4H_2O$ (10) in a field of 1 Tesla (10,000 Oe). The solid line is the calculated plot.

Note: This is a reasonable fit of the data statistically, and reproduces the features of the plots well. The main deviations of the data and fitted line are most likely due to a shifting of the vibrating sample magnetometer (vsm) sample holder during the measurement, as they are sudden, relatively small drops after which the profile continues smoothly.

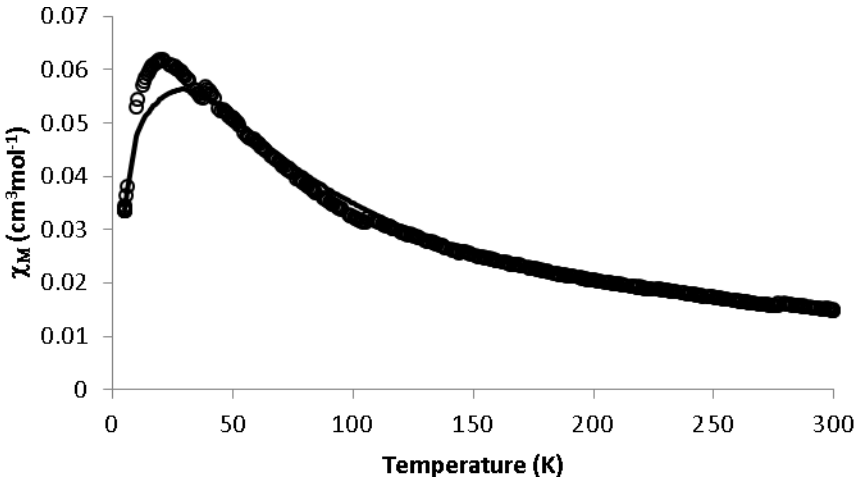

Figure S20: Plot of χ_M, per Ni_4, versus temperature for $[Ni^{II}_4(L^{Et})_2(F)_4](BF_4)_4 \cdot 4H_2O$ (10) in a field of 1 Tesla (10,000 Oe). The solid line is the calculated plot.

Microanalytical data

Table S16: Calculated and found microanalytical data for the tetranuclear complexes 8-12: comparison of X = F^- versus OH^-. Δ = calculated minus found value.

Complex		C (%)	H (%)	N (%)
Fe(II)	Found	48.88	4.32	11.40
$[Fe^{II}_4(\mathbf{L}^{Et})_2(F)_4](BF_4)_4 \cdot {}^5/_2H_2O$ (**8**)	Required (Δ)	48.99 (0.11)	4.57 (0.25)	11.34 (-0.06)
$[Fe^{II}_4(\mathbf{L}^{Et})_2(OH)_4](BF_4)_4 \cdot {}^5/_2H_2O$	Required (Δ)	49.19 (0.31)	4.80 (0.48)	11.47 (0.07)
Co(II)	Found	48.10	4.34	11.16
$[Co^{II}_4(\mathbf{L}^{Et})_2(F)_4](BF_4)_4 \cdot 3H_2O$ (**9**)	Required (Δ)	48.46 (0.30)	4.58 (0.24)	11.30 (0.14)
$[Co^{II}_4(\mathbf{L}^{Et})_2(OH)_4](BF_4)_4 \cdot 3H_2O$	Required (Δ)	48.66 (0.56)	4.80 (0.46)	11.35 (0.19)
Ni(II)	Found	47.78	4.48	11.24
$[Ni^{II}_4\mathbf{L}^{Et}_2(F)_4](BF_4)_4 \cdot 4H_2O$ (**10**)	Required (Δ)	48.05 (0.27)	4.64 (0.16)	11.21 (-0.03)
$[Ni^{II}_4\mathbf{L}^{Et}_2(OH)_4](BF_4)_4 \cdot 4H_2O$	Required (Δ)	48.24 (0.46)	4.86 (0.38)	11.25 (0.01)
Cu(II)	Found	48.30	4.72	10.91
$[Cu^{II}_4\mathbf{L}^{Et}_2(F)_4](BF_4)_4 \cdot 3H_2O$ (**11**)	Required (Δ)	48.02 (-0.28)	4.53 (-0.19)	11.20 (0.29)
$[Cu^{II}_4\mathbf{L}^{Et}_2(OH)_4](BF_4)_4 \cdot 3H_2O$	Required (Δ)	48.21 (-0.09)	4.75 (0.03)	11.24 (0.33)
Zn(II)	Found	48.88	4.33	11.32
$[Zn^{II}_4\mathbf{L}^{Et}_2(F)_4](BF_4)_4$ (**12**)	Required (Δ)	49.17 (0.29)	4.33 (0.00)	11.47 (0.15)
$[Zn^{II}_4\mathbf{L}^{Et}_2(OH)_4](BF_4)_4$	Required (Δ)	49.37 (0.49)	4.56 (0.23)	11.51 (0.19)

^{19}F NMR spectroscopy

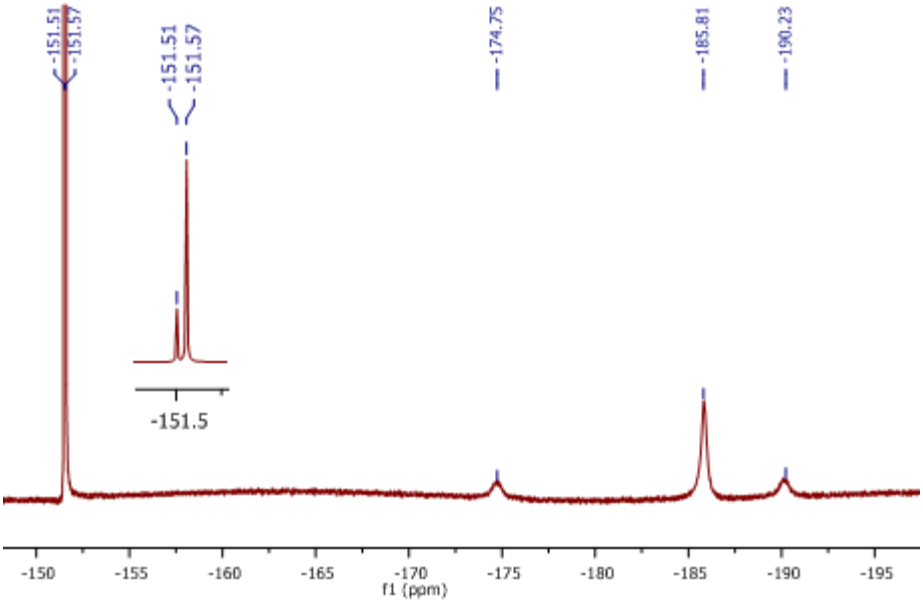

Figure S21: The ^{19}F NMR spectrum of $Zn^{II}_4(L^{Et})_2(F)_4(BF_4)_4$ in deuterated acetonitrile.

IR spectroscopy

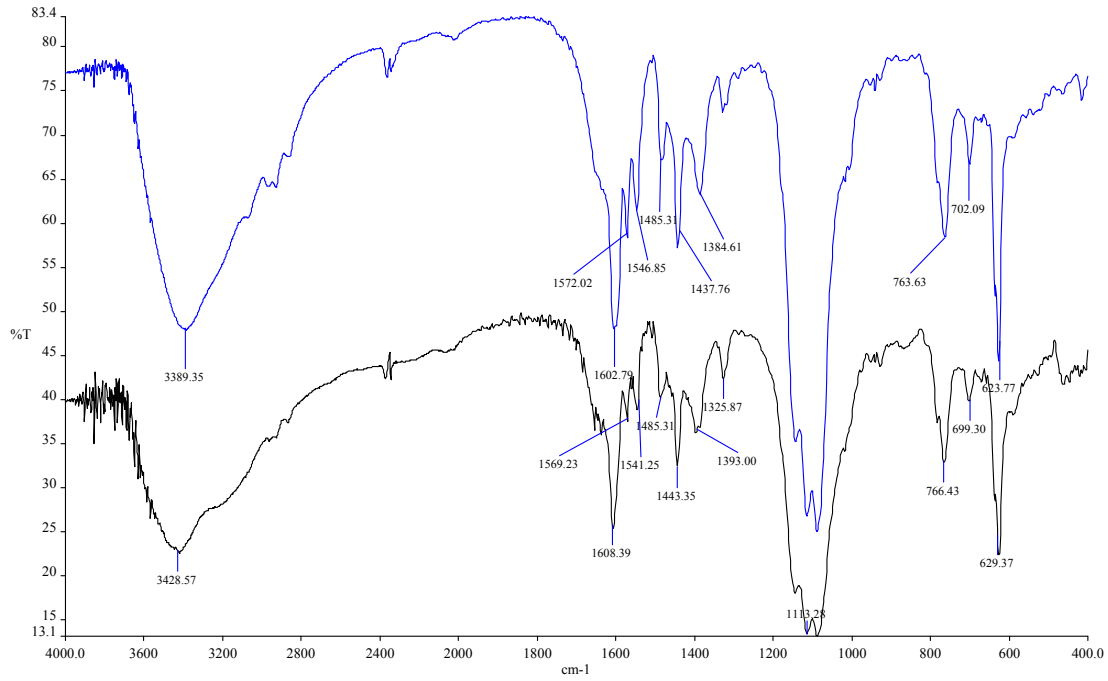

Figure S22: IR spectra of dimanganese(II) complex 1 (bottom, black) and tetramanganese(II) complex 7 (top, blue) in KBr.

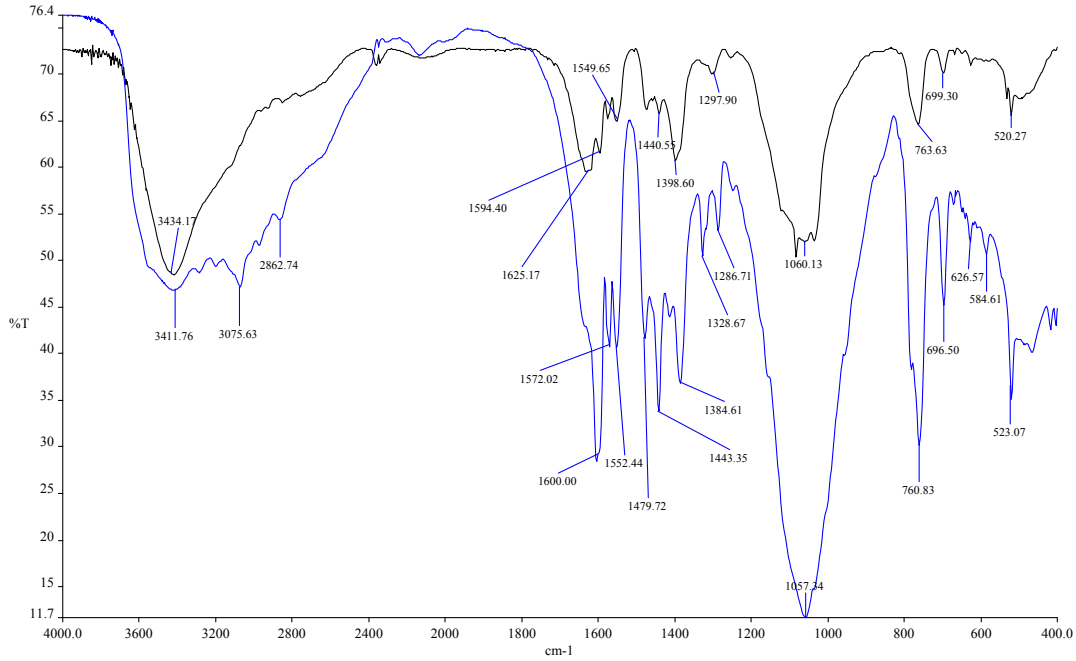

Figure S23: IR spectra of diiron(II) complex 2 (top, black) and tetrairon(II) complex 8 (bottom, blue) in KBr.

References

1 S. Brooker, T. C. Davidson, S. J. Hay, R. J. Kelly, D. K. Kennepohl, P. G. Plieger, B. Moubaraki, K. S. Murray, E. Bill and E. Bothe, *Coord. Chem. Rev.*, 2001, **216-217**, 3.

2 M. Ruben, E. Breuning, M. Barboiu, J.-P. Gisselbrecht and J.-M. Lehn, *Chem. Eur. J.*, 2003, **9**, 291.

3 I. G. Phillips and P. J. Steel, *Aust. J. Chem.*, 1998, **51**, 371.

4 I. G. Phillips and P.J.Steel, *Inorg. Chim. Acta*, 1996, **244**, 3.